Impact Article

Metal cross-linking of helical oligoamide nanorods serves as platform for hierarchical nanofibers

Norton G. West, Rebecca Griffin, Claire Buchanan, Andrew Molino, Alex K. Schenk, Dongchen Qi, Jisheng Pan,* Ljiljana Puskar, Christopher J. Garvey, David J.D. Wilson, Christopher I. Pakes, and Adam Mechler*

Received: 13 August 2024 / Revised: 22 December 2024 / Accepted: 27 January 2025

Helical β-oligoamides serve as versatile molecular building blocks with the unique ability to maintain stable helical fold and be functionalized by sequence modifications without affecting the folding ability. Fibrous head-to-tail self-assembly of these building blocks provides a platform to develop complex nanomaterials. In this study, the metallosupramolecular structure formed by Cu(II) coordination of the $\text{Ac-}\beta^3\text{A}\beta^3\text{V}\beta^3\text{S-}\alpha\text{H-}\beta^3\text{A}\beta^3\text{V}\beta^3\text{A}$ (**1 H**) oligoamide was characterized with spectroscopic, microscopic, and computational methods. Our findings demonstrate that the hybrid sequence leads to a complex helical structure combining a 13-helix on a 14-helix template, stabilized by bifurcated hydrogen bonds. We observe that the **1 H** fibers form in solution, and that copper coordination increases the size of the colloidal structures. When deposited, a homogeneous two-dimensional surface coating was produced, and based on our measurements we are able to propose a structure for the supramolecular framework. These results underline the utility of metallosupramolecular frameworks in bottom-up nanofabrication and nanostructured surface coatings.

Impact statement

Impact statementThis work describes a unique concept in designing hierarchical nanostructured framework-type materials using self-assembly principles. These materials incorporate a combination of head-to-tail supramolecular self-assembly of small helical beta-oligoamide units into nanorods, such as a molecular LEGO system, that are then cross-linked in a specific and geometrically defined way with metal coordination. The resulting materials have a definite internal structure that was assessed with a combination of computer modeling and experimental methods, including atomic force microscopy (AFM), small angle x-ray scattering (SAXS), x-ray photoelectron spectroscopy (XPS), infrared (IR) spectroscopy as well as ultrahigh-resolution STM that made it possible to visualize submolecular details. The ability to form a polynuclear metal complex core in nanoscale fiber bundles in a highly regular but noncrystalline structure opens a range of possibilities for using these materials in, for example, smart fabrics, implants, and potentially molecular electronic and electrooptic applications.

Introduction

Substituted oligoamides, as chemically distinct unnatural analogues of peptides, have been shown to provide a versatile platform for creating complex biocompatible nanostructures given their similarity to natural proteins.[1,2] The advantage of oligoamide chemistry is the ability to combine any amino acid, that is, any molecule with an amine and carboxyl moiety, using well-established solid-state peptide chemistry principles.[3–5] In biological systems α/β-oligoamides have substantial resistance to proteolytic degradation once the β-amino acid content reaches 25–30% of the backbone composition.[6] Therefore, β -oligoamides are prime candidates for intracorporeal applications such as tissue

---

Norton G. West, Department of Biochemistry and Chemistry, La Trobe University, Melbourne, VIC, Australia; Institute of Materials Research and Engineering, Agency for Science, Technology and Research, Singapore, Republic of Singapore
Rebecca Griffin, Department of Mathematical and Physical Sciences, La Trobe University, Melbourne, VIC, Australia
Claire Buchanan, Department of Biochemistry and Chemistry, La Trobe University, Melbourne, VIC, Australia
Andrew Molino, Department of Biochemistry and Chemistry, La Trobe University, Melbourne, VIC, Australia
Alex K. Schenk, Department of Mathematical and Physical Sciences, La Trobe University, Melbourne, VIC, Australia
Dongchen Qi, School of Chemistry and Physics, Queensland University of Technology, Brisbane, QLD, Australia
Jisheng Pan, Institute of Materials Research and Engineering, Agency for Science, Technology and Research, Singapore, Republic of Singapore; Js-pan@imre.a-star.edu.sg
Ljiljana Puskar, Institute for Electronic Structure Dynamics, Helmholtz-Zentrum Berlin für Materialien und Energie, Adlershof, Berlin, Germany
Christopher J. Garvey, Forschungsneutronenquelle Heinz Maier-Leibnitz Zentrum, FRM II and Physik Department E13, Technische Universität München, Garching, Germany
David J.D. Wilson, Department of Biochemistry and Chemistry, La Trobe University, Melbourne, VIC, Australia
Christopher I. Pakes, Department of Mathematical and Physical Sciences, La Trobe University, Melbourne, VIC, Australia
Adam Mechler, Department of Biochemistry and Chemistry, La Trobe University, Melbourne, VIC, Australia; A.Mechler@latrobe.edu.au
*Corresponding author

doi:10.1557/s43577-025-00874-2

scaffolds that can support cell growth;[7–9] *in vitro* results suggest that β-oligoamide-based materials are highly likely to be biocompatible.

The primary structure of an oligoamide is designed through combinations of different amino acid types, α-, β-, or γ-, and the combinations of side-chain residues (i.e., polar, nonpolar, or charged). The oligoamide's primary structure offers a great degree of control of the folding of these sequences into a secondary structure. This directed secondary structure is called a foldamer[1]. The secondary structure of oligoamides is promoted through the intramolecular hydrogen bonding of the backbone amide residues with $i \rightarrow i+n$ configurations, where the periodicity n is known to range from 1 to 6.[10,11] This allows for substantial variation, and therefore designing discrete tertiary structures, in which the geometry of the foldamer and its residues can be predicted and designed has been a long held aim.[1]

β-oligoamides are capable of forming foldamers with five known different hydrogen bonding patterns, these are the 8-, 10-, 12-, 14-, and 10/12-helices.[5,12,13] The 10/12-helix is the most favorable for unsubstituted β-oligoamide; however, the stability is disrupted when the amino acids are substituted, that is, side chains are present, where the 14-helix becomes the most favorable.[13] The 14-helix foldamer formed by β^3-oligoamides is of great interest, due to the ~three β-residues per helical revolution that results in aligned side chains.[12,14,15]

A versatile self-assembling platform is offered by N-acetylation or C-amidation of the oligoamide units, essentially copying the intramolecular hydrogen bonding to the termini, resulting in strong head-to-tail self-assembly into continuous fibers.[16–22] Taking complexity a step further into quaternary structures, in recent works, we have demonstrated metal coordination cross-linking of self-assembled fibrous oligoamides using specific side-chain residues, turning the spontaneously self-assembled oligoamide fibers into two-dimensional (2D) metallosupramolecular frameworks (MSFs).[23,24] The ability to form quaternary structures through metal coordination opens the way for designing complex materials for applications such as molecular electronics, optoactive materials, or surface coatings that promote osseointegration of implants.

A straightforward modification of the reported system, based on Ac-β^3Aβ^3Vβ^3S-αH-αH-β^3Aβ^3Vβ^3A, is varying the number of α-histidine residues. For example, including only one α-histidine with the aim of reducing the previously reported 2D sheets into one-dimensional (1D) assemblies of four nanorods with a polynuclear metal coordination complex core. The oligoamide to achieve this is thus Ac-β^3Aβ^3Vβ^3S-αH-β^3Aβ^3Vβ^3A, henceforth called **1 H**. The structure of **1 H** is given in **Figure** 1, showing the acetylated N-terminus (left), and a protonated form of the carboxylic acid C-terminus. In the current study, we have employed a multifaceted approach to characterize the secondary, tertiary, and quaternary structure of **1 H** as directed by the coordination to Cu^{2+}.

Theoretical calculations were carried out to analyze the modified folding structure and intramolecular hydrogen bonds within the oligoamide. Infrared spectroscopy (IR) was used to glean insights into whether the secondary structure remains intact throughout coordination, and which functional groups are affected: as Cu^{2+} is known to readily denature peptides, the backbone amide bonds are affected if Cu^{2+} causes denaturation.[25] X-ray photoelectron spectroscopy (XPS) was used to probe the oxidation state and chemical environment changes of copper.

Small-angle x-ray scattering (SAXS) data were used to produce a model of the electron-density envelope of **1 H** assemblies in solution, both with and without Cu^{2+}. Atomic force microscopy (AFM) was used to determine tertiary structure of head-to-tail self-assembly, and to observe the morphological changes after copper addition. Scanning tunneling microscopy (STM) was used to look at the fine structure of how the oligoamide self-assembled, both with and without the addition of Cu^{2+} ions.

Results and discussion

Computational study

Molecular topology

The energy minimized structure of **1 H** monomer (**Figure** 2) shows that helical fold is preserved with the inclusion of the α-histidine. The N-terminal loop forms a regular 14-helix; however, the C-terminal loop is distorted to accommodate the additional amino acid. A unique feature is the hydrogen bonding between the imidazole amine and an oxygen of the C-terminal carboxyl, that aligns the imidazole plane parallel to the main axis of the helix. Due to this hydrogen bond, the C-terminal region finds energy minimum by following the helical fold in the monomer, which would potentially interfere with self-assembly. It is more likely that the terminal carboxyl moiety would have to rotate outward to allow the self-assembly to proceed, as it was observed before in crystal structures of self-assembled N-acyl β^3 oligoamides.[22] Therefore, the

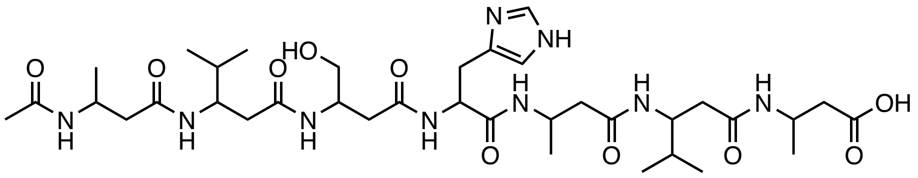

Figure 1. Structure of the oligoamide Ac-β^3Aβ^3Vβ^3S-αH-β^3Aβ^3Vβ^3A, where A is alanine, V is valine, S is serine, and H is histidine.

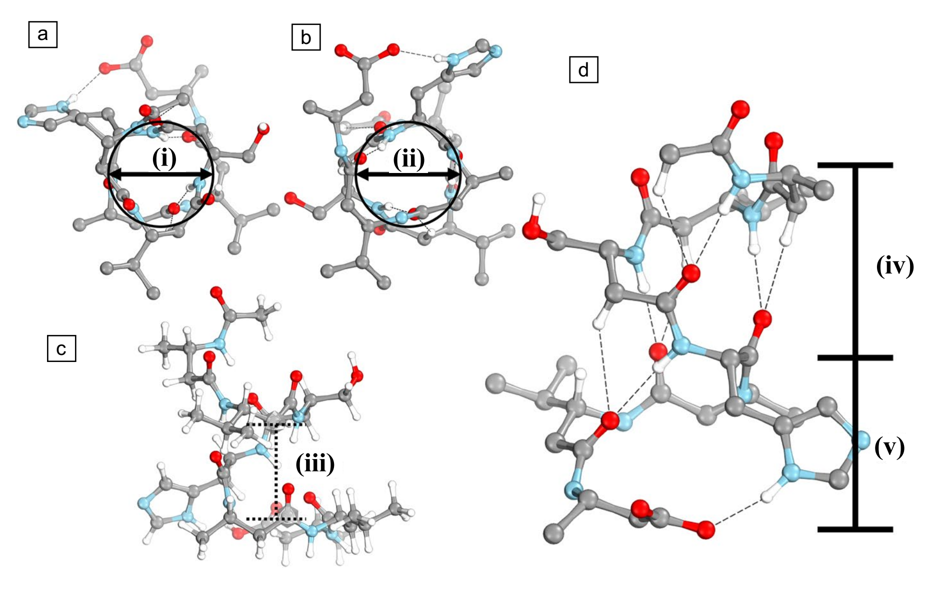

Figure 2. **1 H** energy minimized model. (a, b) are down the helix view from the N-terminus and C-terminus, respectively, showing the location of diameter measurements (i, ii). (c, d) Side views demonstrating main distance between the resulting terminal "disks" (iii) and center of mass, respectively (iv, v). (a),(b), and (d) are shown without hydrogen atoms for structural clarity.

actual monomeric unit in a self-assembled nanorod is expected to be shorter. In a side view, it is apparent that the helix rise also varies due to the distortion, with two low-rise loops at the termini connected by a steep rising segment. The main distance between the resulting terminal "disks" of this structure is approximately 5.5−6.0 Å; that will serve as guidance for interpreting scanning tunneling microscopy (STM) images.

Quantum theory of atoms in molecules

Quantum theory of atoms in molecules (QTAIM) calculations were conducted to assess the influence of hydrogen bonding on the structure of **1 H**. Five bond-critical points (BCPs) were identified, associated with three-point bifurcated hydrogen bonds in β^3-alanine, β^3-valine, β^3-serine, and across the amide group of α-histidine. These BCPs describe a Cα–H donor group in the residues immediately N-terminal to those bearing the N–H donor group. In this arrangement, both donor groups share a common C=O group as an acceptor (**Figure** 3).

Table I lists the QTAIM properties for these BCPs. The Laplacian of the electron density, $\nabla^2\rho$, indicative of electron-density accumulation between two atoms, serves as the predominant metric for assessing hydrogen bond strength. Typical $\nabla^2\rho$ values for hydrogen bonds range from +0.2 to +0.14 a.u.[26,27] In **1 H**, the N–H–O BCPs exhibit $\nabla^2\rho$ values that fall within the typical range for hydrogen bonding interactions. In contrast, Cα-H–O bonds demonstrate lower $\nabla^2\rho$ values (+0.007 to +0.021 a.u.). These reduced values are in line with expectations given the minimal polarization characteristic of C–H bonds. In group 1, the terminal Cα–H–O interaction fails to meet the hydrogen bonding criteria across all measured metrics. Conversely, in groups 2, 3, and 4, the BCPs associated with methylene Cα–H–O interactions indicate weak bonding interactions. The computed anisotropy of the electron density, indicated by |1|/3, corroborates these findings. Specifically, the |1|/3 value for the Cα–H–O BCP in group 1 is negligible. In contrast, the |1|/3 values for the methylene Cα–H–O BCPs in groups 2, 3, and 4 are approximately half of those observed for the corresponding N–H–O BCPs in the same bifurcated hydrogen bonds. Additionally, the delocalization index (DI) for methylene Cα–H–O BCPs indicates a nonnegligible bonding interaction, albeit weaker than N–H–O hydrogen bonds. The electronic energy density term, *H*, quantifies the contribution of electronic energy to the stabilization of bonding interactions. Although the values of *H* are greater for the BCPs of N–H–O bonds, the cumulative contribution of Cα–H–O bonded interactions, in addition to the formal N–H–O hydrogen bonds, should not be underestimated. The QTAIM analysis highlights the integral role of both N–H–O and Cα–H–O bonding interactions in **1 H**, suggesting that the cumulative effect of the weaker Cα–H–O bonds plays a role in determining its stability and conformation.

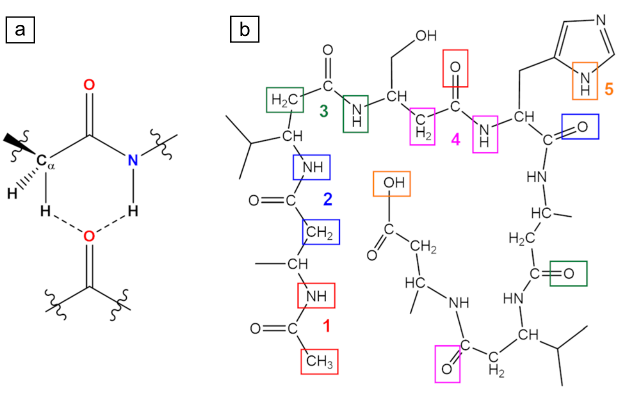

Figure 3. (a) Three-point bifurcated hydrogen bonding. (b) Color-coded hydrogen bonding groups.

Table I. Electron-density topological and integrated atomic properties of quantum theory of atoms in molecules QTAIM calculations.

	XH–O Bond	q(X)	q(H)	q(O)	$\nabla^2\rho$(H–O)	|V|/G	H(H–O)	|1|/3	DI(H–O)
Group 1	CH–O	−0.050	0.024	−1.236	0.007	0.603	5.06E–04	0.147	0.005
	NH–O	−1.238	0.454	−1.236	0.018	0.737	9.44E–04	0.161	0.020
Group 2	CH–O	−0.010	0.025	−1.223	0.019	0.755	9.58E–04	0.164	0.020
	NH–O	−1.232	0.452	−1.223	0.065	0.948	7.97E–04	0.200	0.055
Group 3	CH–O	−0.011	0.024	−1.233	0.021	0.779	9.70E–04	0.161	0.024
	NH–O	−1.232	0.448	−1.233	0.047	0.907	1.00E–03	0.184	0.039
Group 4	CH–O	−0.007	0.017	−1.240	0.018	0.729	9.33E–04	0.160	0.018
	NH–O	−1.215	0.461	−1.240	0.061	0.926	1.06E–03	0.192	0.049
Group 5	NH–O	−1.299	0.456	−1.135	0.049	0.980	2.39E–04	0.209	0.046

As the helicity of a foldamer is defined by the number of atoms contained within the hydrogen bonding ring, the stronger of the two bifurcated hydrogen bonds was used to determine helicity. The N-terminus loop of group 1 is a 14-helix, groups 2–4 which make up the majority of **1 H** are 13-helix. This is likely due to the degree of steric hindrance introduced from the α-histidine, as the amide oxygen hydrogen bond acceptors are after the α-histidine in the oligoamide sequence (Figure 3). BCP group 5 demonstrates that the addition of α-histidine also provides a hydrogen bonding pair between the imidazole and C-terminus carboxyl moities. This BCP is as significant as the intramolecular hydrogen bonds of groups 1–4 for the secondary structure of **1 H** (Table I). Group 5 forms a 19-membered ring, which is larger than the other BCPs. This is consistent with the energy minimized structure of Figure 2 as the C-terminus was measured to be larger in diameter than the N-terminus. The proximity afforded by the hydrogen bonding of histidine and carboxylate indicates that both moieties can be involved in bidentate coordination to the same copper center. This was explored with XPS to determine if the imidazole and glutamic acid have the same affect on $CuCl_2$ as **1 H**.

QTAIM analysis demonstrated the five sets of intramolecular hydrogen bonds that stabilize the helix of **1 H**, illustrated in **Figure** 4. To ensure that this secondary structure is preserved throughout the copper addition, one can look at the vibrational modes of the backbone amides to determine if this secondary structure is preserved.

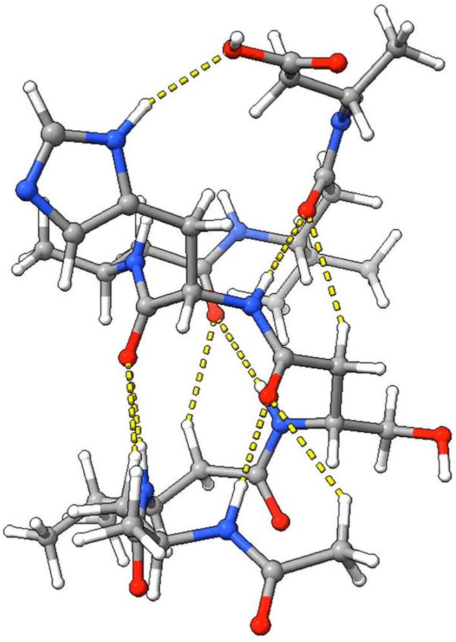

Figure 4. **1 H** visualization showing calculated hydrogen bonding pairs.

Spectroscopy

Spectroscopic methods for characterizing **1 H** + Cu allow for gleaning ensemble information about the sample that is reliable for characterization of the chemical changes that are occurring through $CuCl_2$ coordination to **1 H**.

Infrared spectroscopy

IR reveals the functional groups present within **1 H** and their change upon the copper addition process. Spectra are shown in **Figure** 5; peak assignments are summarized in **Table** II In mid-IR (MIR) spectra the amide I and II bands at 1644 cm^{-1} and 1548 cm^{-1}, respectively, are useful markers of secondary structures. The amide I band is predominately from the C=O stretch vibration of the amide backbone, whereas the amide II band is a composite band of N–H bending and C–N stretch modes, also from the carbon backbone.[28,29] As such, these bands are sensitive markers to any change in the secondary structures of substituted oligoamides. These peaks were not affected by the addition of copper, confirming that the backbone amide moieties are unaffected by coordination and the helicity is preserved (see Figure 5).

A small peak at 1721 cm^{-1} can be assigned to the carboxylate vibration modes. This peak narrows after the addition of copper indicating that the carboxylate moieties in **1 H** align to more consistent environments after the MSF formation process.

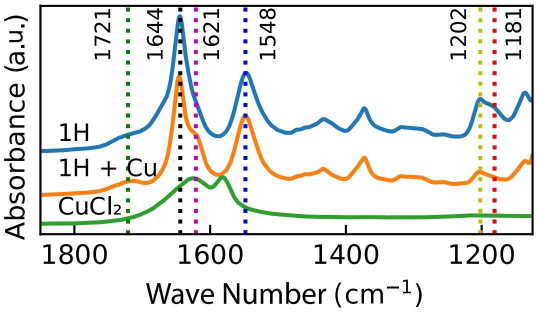

Figure 5. Representative mid-infrared Fourier tranform-infrared spectroscopy spectra: **1 H** before (top) and after $CuCl_2$ addition (middle), and neat $CuCl_2$ (bottom).

Table II. IR assignments.

Wave Number	Assignment	Change
1721 cm^{-1}	Carboxylate COO^{-}	Narrowed
1644 cm^{-1}	Amide I (backbone)	No Change
1621 cm^{-1}	Metal–Salt hydration	Appears
1548 cm^{-1}	Amide II (Backbone)	No Change
1202 cm^{-1}	(CN) (NH)	No Change
1181 cm^{-1}	His (CN) (NH)	Disappears

The band at 1621 cm^{-1}, present only in the $CuCl_2$ control and **1 H** + Cu spectra, can be assigned to metal–salt hydration. Unlike the AFM and XPS experiments where excess $CuCl_2$ was removed through rinsing, excess $CuCl_2$ was not removed to ensure the amount of **1 H** on the ATR crystal would not change, which would affect peak intensity. The significant change between the spectra is the disappearance of 1181 cm^{-1} for **1 H** + Cu, which was previously assigned to the histidine (CN) (NH) vibration mode indicating deprotonation of the imidazole amine of the histidine side chain.[30] This deprotonation indicates coordination of copper to the imidazole ring of the histidine Table II.

XPS

XPS reveals information about the chemical environment for and around the copper that was added to **1 H**. **Figure** 6a shows the presence of Cu^{2+} as indicated by the presence of the satellite peak around 943 eV. The presence of Cu^{2+} is also supported by the shoulder peak observed at 934.6 eV.[31] The main $2p_{3/2}$ region is dominated by a peak at 932.6 eV, which can be either Cu^{0} or Cu.$^{1+}$ [31] This uncertainty means that the Cu2p photoelectron peak alone cannot characterize the oxidation state of copper[31], and so the copper $L_3M_{4,5}M_{4,5}$ Auger transition (Figure 6b) has also been measured, as this is more sensitive to the oxidation state.[32]

Before rinsing the sample the LMM peak was located at 915.2 eV, which is consistent with Cu^{1+} [33], that is, Cu^{2+} is reduced to Cu^{1+} when coordinated to **1 H**.

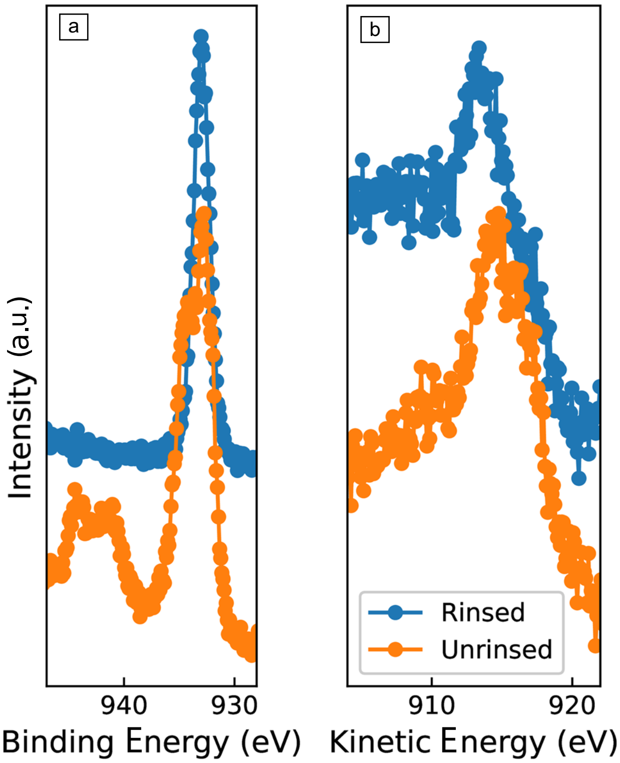

Figure 6. X-ray photoelectron spectroscopy spectra from before and after rinsing **1 H** + Cu: (a) Cu $2p_{3/2}$ (b) Cu Auger $L_3M_{4,5}M_{4,5}$ transition.

After rinsing, the Cu $2p_{3/2}$ peak is present at 933.0 eV. The rinsing process definitely removed any residual Cu^{2+}, as also confirmed by the absence of the characteristic satellite peak.[31] The Cu Auger peak was found at 914.8 eV, which is lower than the unrinsed **1 H** + Cu. The Cu Auger peak position was closer to Cu^{1+} than Cu^{0} and Cu^{2+}.

Plotting Cu $2p_{3/2}$ and $CuL_3M_{4,5}M_{4,5}$ peaks of each sample in a scatter plot (Figure 6) allows for characterization of the chemical environment of the copper coordination center. This is known as a Wagner plot.[34] Data point groupings within the Wagner plot reveal similar chemical environments.[34]

The copper Wagner plot in **Figure** 7 contains data sets from repeats of experiments as well as reference measurements of $CuCl_2$ from the same batch that was used to coordinate with **1 H**, and the locations align with the expected Cu(II) grouping from the NIST database.[33]

Control experiments with imidazole and glutamic acid were also conducted to correlate Cu chemical environment with the binding moities identified previously.[23] Imidazole and glutamic acid both reduce Cu^{2+} in a similar shift from neat $CuCl_2$ to **1 H** + Cu. This means that both functional groups of the histidine's secondary amine, and glutamic acid's carboxylate can be involved in coordination between **1 H** and copper. The deprotonation of histidine as identified by IR spectroscopy in Figure 2 is likely involved in the mechanism of reduction of Cu^{2+}.

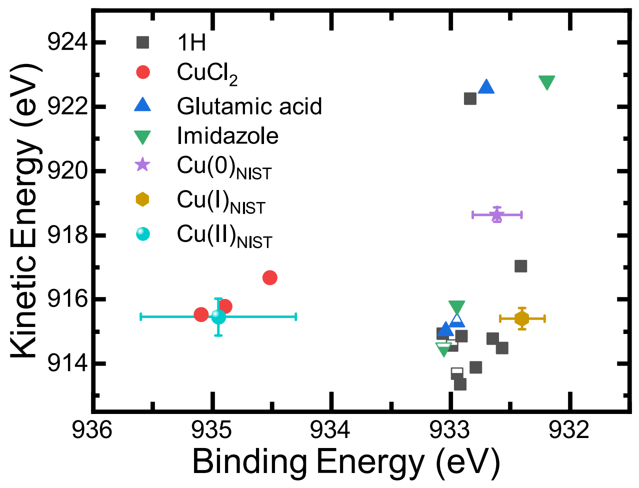

Figure 7. Copper Wagner plot.

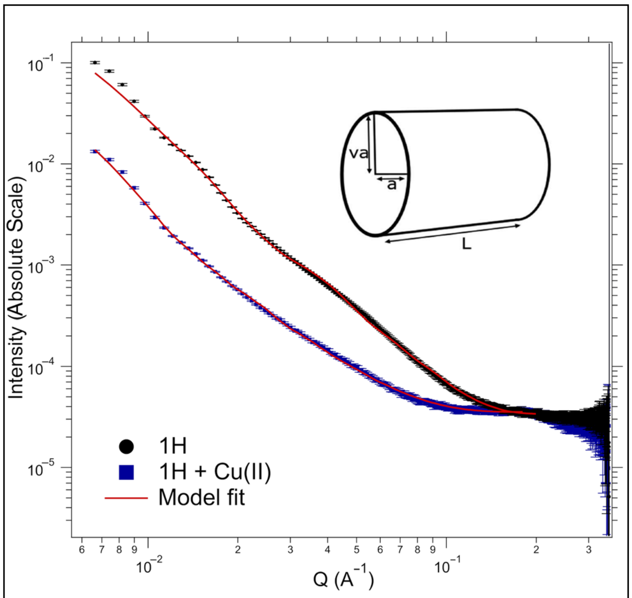

Figure 8. Results from small-angle x-ray scattering experiments, showing populations of size distributions.

Table III. Data from the SAXS model fits, showing the calculated sizes for the two elliptical cylindrical models with associated error.

Population	Radius Minor Axis	Radius Major Axis	Length
1; 1 H	12.24 0.03 nm	36.56 0.53 nm	641.74 9.61 nm
2; 1 H	1.77 0.01 nm	6.48 0.09 nm	314.60 12.26 nm
1; 1 H + Cu	22.27 0.25 nm	38.09 1.18 nm	169.14 2.32 nm
2; 1 H + Cu	2.12 0.05 nm	19.08 1.13 nm	66.33 2.31 nm

The grouping of datapoints corresponding to high kinetic energy were found in samples where two Auger peaks were observed; these peaks retain the characteristic broad $CuL_3M_{4,5}M_{4,5}$ line shape. There are no corresponding overlapping regions for other elements present in this energy range, as determined by the survey spectra. The position and shape of these high kinetic energy peaks is, however, consistent with metallic copper, and therefore, their presence suggests that in some, but not all, of the samples the reduction of copper proceeds to Cu(0) while retaining a population of Cu(I) as well, suggesting the presence of two distinct chemical environments for coordination. While a similar effect was observed before for **2 H** oligoamide,[23] in the case of **1 H,** it was not expected due to the more restrictive coordination geometry of the single histidine residue per oligoamide unit. Therefore, it is possible that **1 H** can have two chemically different superstructures upon coordination.

Molecular topology analysis

Through the understanding of the theoretical structure and spectral behavior of **1 H** + Cu, experimental characterization of the structure can be continued with more gravitas.

SAXS

SAXS was used to investigate the electron-density envelope of the oligoamides in solution. It was also used to determine the fiber geometry in solution before and after $CuCl_2$ addition. SAXS data are shown in **Figure** 8. The model used was based on a composite model of two elliptical cylinders, indicating two size populations in each sample (see Supplementary information). The elliptical cylinder model is suitable to determine the cross section of the fibers; however, it must be noted that due to the highly variable nature of the head-to-tail assembly motif, the value for the length of the cylinders represents the average of a broad distribution and therefore it is not a reliable indicator for any meaningful insights. Therefore in the analysis of these data only the cross-sectional radii are considered. Fitting found that there are two distinct size populations (**Table** III). In both cases, the large difference between the minor and major axes of the ellipse suggests flat, ribbon-like structures (nanoribbons). Population 1 is consistent with bundles of oligoamide fibers that form in solution due to polar/dispersion interactions. Population 2 is much smaller, with dimensions indicating that it consists of only a few oligoamide nanorods (versus theoretical helix diameter of ~0.5 nm as previously shown).

Once copper was added to the **1 H** solution, there was a notable increase in the dimensions, indicating a strong lateral interaction between fibers in both populations (Table III). The near doubling of sizes in the smaller population indicates the coordination attachment of individual nanoribbons in either direction, whereas the larger bundles have seen a doubling only in the minor axis suggesting that the larger structures can also attach, but increasing the thickness is energetically favored. Lack of a broadening of

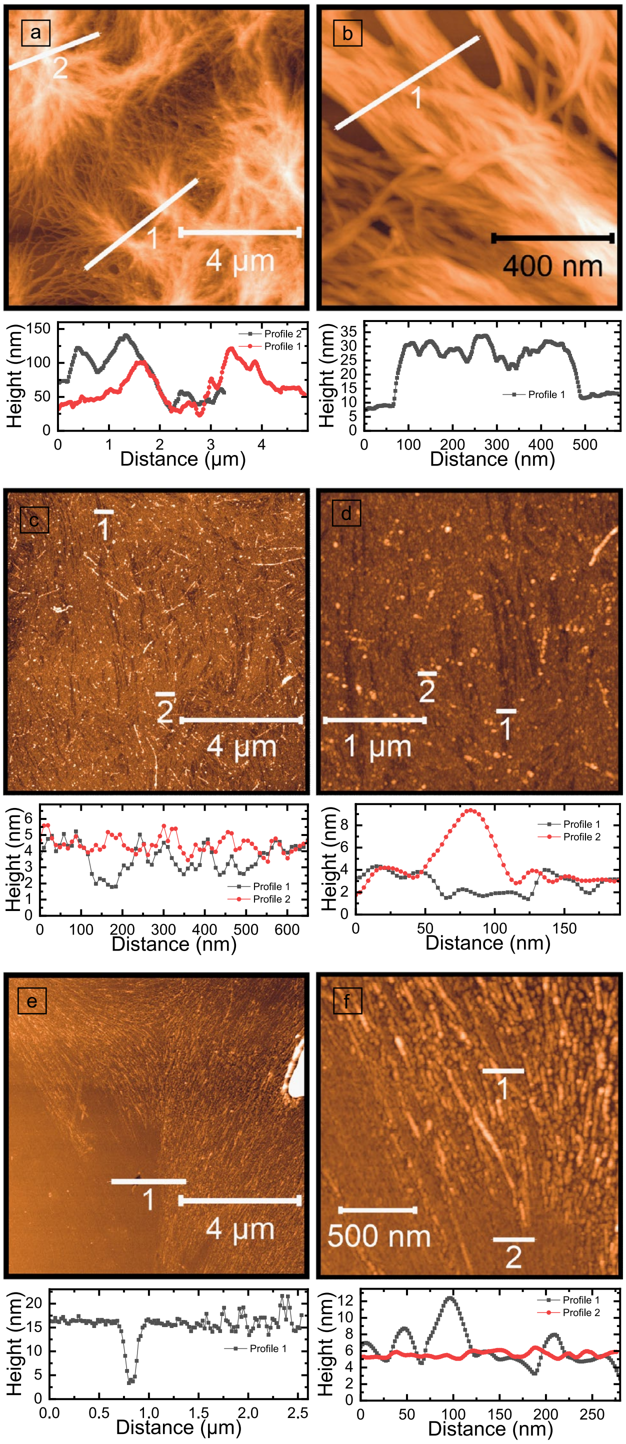

Figure 9. Atomic force microscopy images and corresponding line profiles of: (a, b) **1 H**, (c, d) **1 H + Cu**, (e, f) **1 H + Cu** after rinsing.

Table IV. Measured features corresponding to line profiles of Figure 9.

Panel	Profile #	Feature (nm)
(a)	1	60 7
	2	72.8 19
(b)	1	17.7 4.8
	1 (top)	5.4 1.04
(c)	1	2.2 0.58
	2	0.96 0.08
(d)	1	1.4 0.7
	2	5.5 0.49
(e)	1	12.5 0.39
(f)	1	5.95 1.1
	2	1.1 0.1

the distribution suggests that the attachment of the smaller nanoribbons to the larger bundles is less likely, potentially indicating different packing in the two structures. The data confirm that coordination takes place in solution between already assembled structures, but it also suggest that these structures do not break up to form a new network, at least initially. Therefore, more regular, nanorod-level attachment is more likely to proceed with monomers and small oligomers upon drying. These smaller structures are invisible in SAXS, but still contain a large amount of material as it was shown before[21] (**Figure** 8).

AFM

AFM has been used to investigate the surface morphology of the oligoamide fibers throughout the process of metal addition and subsequent washing.

Figure 9a–b depicts **1 H** after deposition showing fibrous assemblies at a length scale of greater than 10 µm. This demonstrates a lateral affinity between different oligoamides likely due to weak intermolecular forces, as the fibers roughly bundle into larger structures. Figure 9a shows that the height[1] of the bundles are ≈65 nm, as reported in **Table** IV. In contrast, Figure 9b shows a ≈15-nm-thin bundle, whereas the superimposed fine features are ≈5-nm tall. The dimensions correlate well with the SAXS measurements, although they do not match exactly. Knowing the average diameter of **1 H** is ≈0.5 nm, the AFM indicates the fine structure comprises up to ~10 parallel oligoamides.

Figure 9c–d shows **1 H** + Cu structures with less height variation, but much increased lateral dimensions across the sample. The thin film of **1 H** + Cu is flat with features of ≈1-nm tall, and crevasses ≈1.5-nm deep (Table IV [c, d]). This layer shows incomplete parallel alignment due to the presence of the crevasses. **1 H** + Cu also shows randomly aligned protofibers, with a height of ≈5 nm (Table IV [d]), which is consistent with the fine features of **1 H**. The rinsing of **1 H** + Cu seen in Figure 9e–f produces a tightly packed layer without randomly aligned material on top. The thickness of this layer was determined to be ≈12.5 nm. This is likely due to rinsing allowing for a rearrangement of **1 H** to promote

---

[1] As the oligoamides are parallel to the substrate, the height measured corresponds to the diameter. Therefore, the SAXS minor radius needs to be doubled for comparison to AFM height.

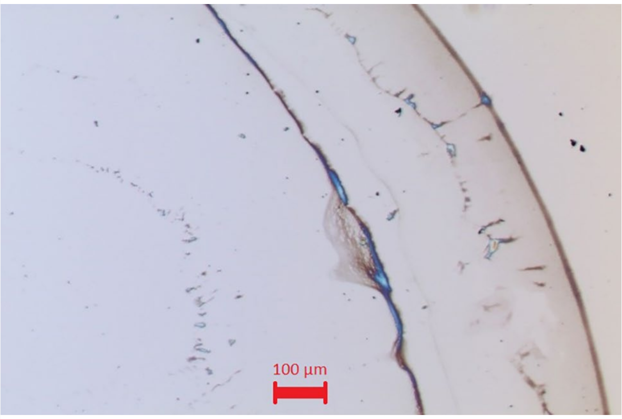

Figure 10. Confocal microscope image shows **1 H** + Cu after washing.

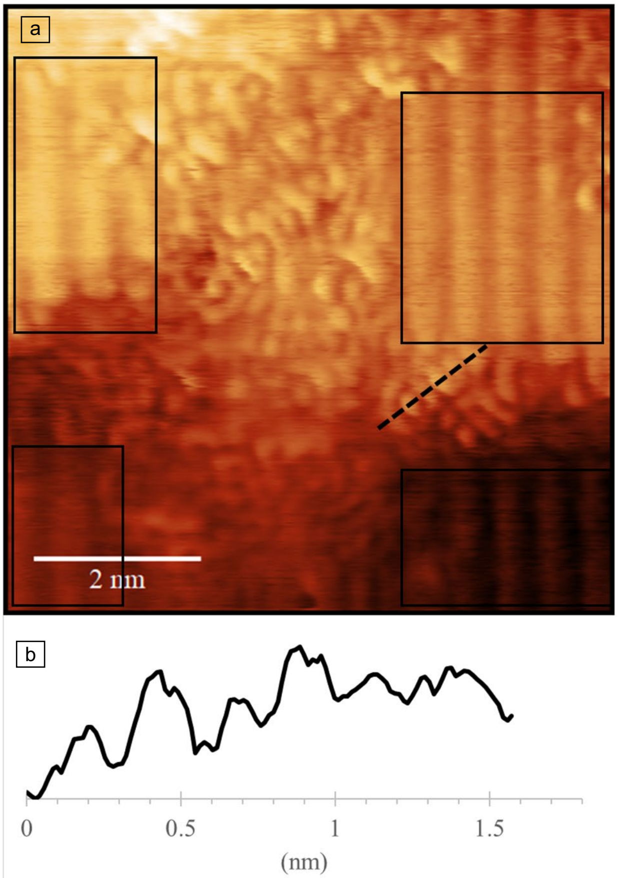

Figure 11. (a) Scanning tunneling microscopy scan after **1 H** deposit. The regions marked with boxes indicate diamond substrate. The marked line runs along the length of a suspected **1 H**. (b) Profile along the marked line in (a). The separation between peaks has an average value of 0.24 nm ± 0.024 nm.

complete parallel alignment, while also removing loose material, including uncoordinated $CuCl_2$ (as confirmed by XPS). Figure 9e shows domains of aligned protofibers on top of the tightly packed **1 H** + Cu layer. This is confirmed by Figure 9f, which shows a ≈6-nm protofiber, without crevasses that were observed previously.

A confocal microscope image (**Figure** 10) shows the oligoamide after metal coordination and washing. The center shows both curious colored regions and larger macroscopic fibrous structures. These colors are possibly indicative of optical activity due to delocalized electrons within the MSF.

While the AFM measurements indicate a tightly packed deposit is formed after the addition of copper, we are unable to observe any details of the underlying atomic-scale mechanism due to the limited resolution of AFM. To gain more information we turn to STM, which can be used to probe some of the atomic-scale structures that allow the alignment seen after copper addition.

STM

STM was used to investigate atomic resolution oligoamide alignment on hydrogen-terminated diamond. A hydrogen-terminated C(100) diamond surface typically has a 2 × 1 reconstruction; this forms terraces.[35] The 2 × 1 reconstruction is shown in **Figure** 11a, the two diamond terraces are outlined by the boxes, which are separated by amorphous carbon. The region identified by the line profile (dashed black line) is not diamond as it does not match with well-known diamond morphology nor have the appropriate symmetry for this substrate. In addition, it is likely not amorphous carbon due to the regularity of structure. Therefore, the line profile of Figure 11b is potentially isolated **1 H**; this demonstrates the preservation of the helical assembly and head-to-tail-motif while deposited on hydrogen-terminated diamond.

The line profile of Figure 11b shows that the separation between the ridges of the oligoamide is ~0.24 nm. This suggests multiple oligoamides self-assembled along the surface. The topological analysis of the energy minimized structure suggested that the distance between the terminal loops of the helix was >~0.5 nm and therefore, the periodicity recorded here is roughly half of that distance. However, it should be noted that the ridges show two distinct heights, one lower and the next taller, and the difference between the taller ridges is approximately 0.5 nm. Noticing that the steep rising loop connecting the terminal loops passes approximately halfway between the two terminal disks (cf. Figure 2), the spacing is consistent with the dimensions of the helix laying on its side, and that the STM captured an oligoamide head-to-tail dimer in this image.

Figure 12 shows a scan after the addition of Cu(II) to **1 H** and rinsing of the sample. A tightly packed layer was observed that is consistent with the fiber alignment seen in AFM scans of equivalent deposits (Figure 9e–f), which posits a tightly packed layer. The scan can be roughly divided into three regions separated by the diagonal dashed lines. Region (i) (Figure 12) shows a degree of disorder that is

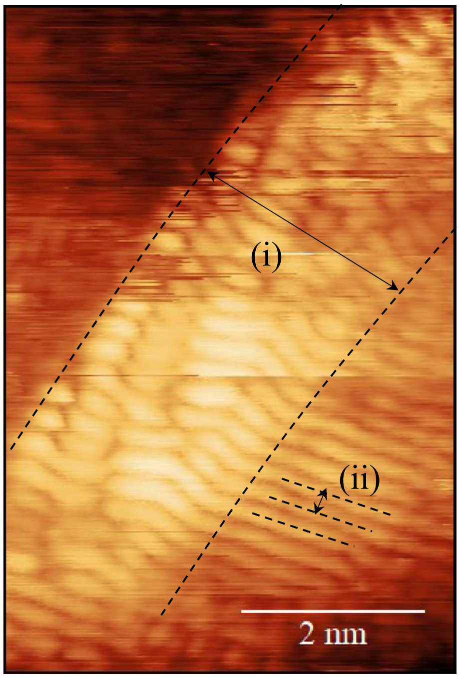

Figure 12. Scanning tunneling microscopy of **1 H** + Cu after rinsing, demonstrating a tightly packed layer. (i) Marks a measurement across the suspected fiber and has a value of around 2 nm. (ii) Marks a representative measurement between ridges of the tightly packed region, and has an average value of 0.23 nm ± 0.015 nm.

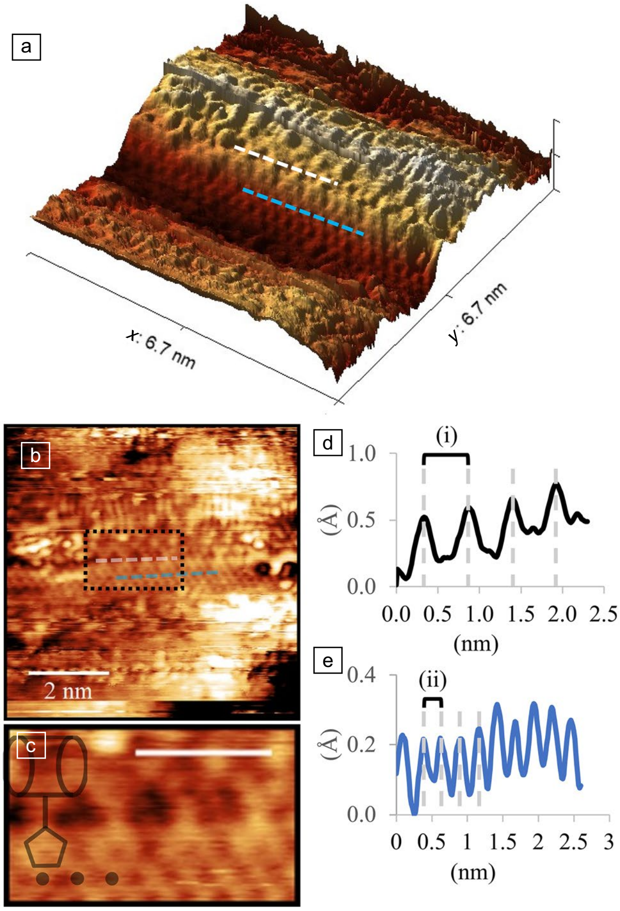

Figure 13. Scanning tunneling microscopy (STM) of coordination site. (a) Three-dimensional projection of bundle with line plots marked. (b) Orthogonal projection of the same STM image shown in (a), with line plots and region of (c) marked. (c) Zoomed region with proposed coordination structure overlaid. Scale bar = 1 nm. (d) Line profile across oligoamide, (i) shows an average peak separation of 0.53 nm. (e) Line plot across potential coordinated copper atoms, (ii) marks an average peak separation of 0.26 nm ± 0.018 nm.

consistent with bundling of the nanorods into a superhelix at the edge as the layer frays. The central region of (i) Figure 12 shows a “braided” structure that runs diagonally across the image. The width of braided region (i) spans a length of around 2 nm, which matches fairly well with the SAXS measurement of the **1 H** minor radius following metal coordination (Table III).

The rightmost region is highly ordered, the row structures bear resemblance to diamond surface structures; however, since dimer rows run horizontally and vertically on this substrate (Figure 11), we infer that these structures are **1 H**. The ridges marked by dashed lines labeled (ii) have a separation of 0.23 nm ± 0.015 nm. This separation is highly consistent with the observation on the noncoordinated sample (Figure 11) and because of this, these structures could be interpreted as a highly ordered layer of oligoamides, with the fibers running in the plane of the sample and perpendicular to the marked ridges, and lateral ordering facilitated by Cu(II). This tightly assembled layer indicates that Cu(II) addition is responsible for “zipping up” the oligoamides into the MSF structure. As no distinct surface features can be observed for copper coordination in Figure 12, we believe that the copper coordination centers are residing within the layer, and are therefore, obscured by the surrounding fibers.

Figure 13 shows an STM scan over a different region of the **1 H** + Cu sample. The three-dimensional view shown in Figure 13a indicates a fiber-like structure running parallel to the *x*-axis. This structure has a width of ~3 nm, which agrees well with the SAXS measurement of **1 H** + Cu minor radius (Table III). The bonding indicated by Figure 13 isn’t typical of **1 H** + Cu; however, this region allows us to probe the coordination geometry.

Figure 13b shows an orthogonal projection of the same STM scan, where the curve of the fiber has been removed by background subtraction to provide a clearer view of the ordered structures present on the side of the fiber structure. The surface texture of the **1 H** fiber in Figure 13 is different from that in Figure 12, in particular the exposed “lattice” on the side of the structure in Figure 13 is not seen. This could be because the structure is hidden by the continuous 2D layer seen in Figure 12, or due to a different bundling arrangement from the main population (cf. proposed scheme **Figure** 14). The bonding

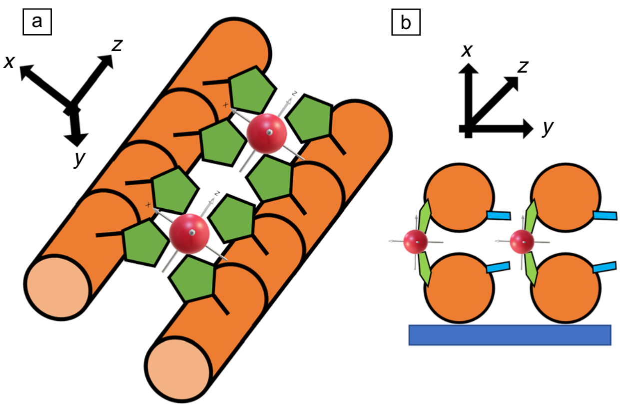

Figure 14. Proposed structure of metallosupramolecular framework, showing **1 H** as orange cylinder, histidine as green pentagon, and copper as red sphere. (a) Isometric view of proposed structure. (b) Front view of proposed structure, with serine as the light blue small rectangle, and the substrate as the large blue rectangle.

arrangement depicted in Figure 13, while allowing a unique insight of a specific coordination arrangement, is likely not representative of the majority of coordination sites.

Figure 13c is a close-up view of (b), where the ordered structures are clearest, and has a proposed structure overlaid. The two dashed lines in Figure 13a–b are in the same position on both images, and mark the two distinct structures visible on the side of the fiber. The top line corresponds to the line plot in Figure 13d, and marks "y" structures, which have a separation of around 0.53 nm. The bottom line corresponds to the line plot in Figure 13e, and marks "lattice" structures. These have a separation of 0.26 nm ± 0.018 nm. This pattern can be explained with incomplete coordination of an oligoamide with Cu(II) that incidentally allowed STM imaging of the coordination network.

The line profile of Figure 13d is placed across suspected histidine residues, where the separation of 0.53 nm is in loose agreement with the length of the helical monomer **1 H** (~0.55–0.59 nm as per above). The line profile across the fine structure (Figure 13e) shows an average peak separation of 0.26 ± 0.018 nm, which is close to a Cu–Cu bond length of 0.244 nm that has previously been measured on a freestanding 2D copper monolayer.[36] Therefore, the **1 H** oligoamide is potentially fostering the formation of Cu–Cu bonds within the MSF network.

Discussion

To summarize the main findings, the experimental structural data confirms that the helix and head-to-tail self-assembly is preserved throughout copper coordination. The single histidine per unit was intended to create bundles of four nanorods, yet the structures appeared 2D. STM has shown what appears to be a network of histidine residues coordinating to metal centers along the main axis of the nanorods. We interpret this arrangement to mean that the nanorods are acting as bidentate ligands with both nitrogen atoms, atoms with the amine nitrogen being activated by deprotonation. In contrast, the arrangement of **1 H** + Cu was expected to be similar to the proposed structure of **2 H** + Cu,[23] whereby four oligoamide foldamers coordinate around one copper center and individually form square-planar complexes. The mechanism for the foldamers to form a square-planar complex is dependent on the alignment of the imidazole group of histidine, which is initially provided by the hydrogen bond to the C-terminus that templates each foldamer to have the histidine aligned tangentially. Each templated foldamer is then prepared to form the same coordination geometry with the introduced copper. As the coordinated copper is between four histidine residues in this parallel arrangement, a square-planar geometry is adopted. Figure 14a is an illustration of this proposed structure. Figure 14b is a view of a substrate supported **1 H** + Cu MSF. As the serine residue is opposite the histidine (Figure 1), the arrangement allows for serine to bind to the out of plane copper orbitals, which in turn, causes each set of coordinated fibrils to align and zip up into the observed 2D MSF network.

Conclusion

The MSF forming ability of the Ac-β^{3}Aβ^{3}Vβ^{3}S-αH-β^{3}Aβ^{3}Vβ^{3}A (**1 H**) oligoamide was established using copper as the test metal. The theoretical calculations of **1 H** with QTAIM revealed that the helix varies from a 14-helix at the N-terminus, to a 13-helix in the middle section, and a 19-helix at the C-terminus in conjunction with the α-histidine. The hydrogen bonding of histidine and the C-terminal carboxylate provides a template for longitudinal square-planar coordination along the **1 H** nanorod. Cu^{2+} was reduced mostly to Cu(I) upon coordination to **1 H** ($Cu^{2+} \rightarrow Cu^{1+}$), as derived from spectroscopic analysis.

Structural analysis of **1 H** demonstrated the head-to-tail self-assembly motif is intact considering the altered helix structure, allowing for formation of fibrous assemblies. **1 H** also demonstrated an increase in the degree of how interconnected the fibrous assemblies become due to metal coordination. STM enabled observation of the electron density of a single oligoamide helix and the coordination network alongside. The ability of the β-oligoamide **1 H** to form a thin layer material on surfaces warrants future studies into the biocompatibility for osseointegration applications.

Materials and methods

Computational methods

Energy minimization

Energy minimization was performed in two steps. First, the peptide was screened with the Spartan software (Wavefunction Inc. Irvine) for the conformer with the lowest electronic energy. Consecutively, the structure was optimized with the B3LYP/6-31+G(d) model chemistry using the Gaussian 09 software package.[37] The starting point of the energy minimization employed a modified PDB file from crystallographic data collected of an analogous β3 oligoamide. Energy minimization was used to approximate the oligoamide's preferred confirmation.

QTAIMs

QTAIM calculations were performed using the Proaim integration method and a fine interatomic surface as implemented in the AIMALL (19.10.12) suite of programs.[38] Accuracy of the integration process was confirmed with a threshold of 10^{-4} a.u. for the atomic integrals of the one-electron density of the Laplacian within all atomic basins. The summation of all basins energies was compared with the total electronic energy of the molecules, calculated independently at the B3LYP/6-31+G(d) level of theory, to confirm the differences remained below a threshold of 1 kcal/mol.

Infrared spectroscopy

Mid-IR measurements were carried out in the infrared laboratory at Helmholtz-Zentrum Berlin. A Bruker VERTEX 80v spectrometer, kept at a vacuum of 3.0 hPa to <1 hPa, was operated with a liquid nitrogen-cooled MCT detector and KBr beamsplitter in an ATR single bounce collection mode (Si ATR crystal). The ATR sample holder has the option of varying the relative humidity (RH) of the sample environment.

IR sample preparation

Lyophilized **1 H** powder was dissolved in isopropanol, then drop-cast onto Si ATR crystals. De-ionized (DI) water was used to hydrate the oligoamide and promote self-assembly on the ATR crystal. After hydration with DI water, the sample was dried with purging dry nitrogen through the enviromental cell. The water stretch (3400 cm^{-1}) and water bend (1630 cm^{-1}) bands were observed and reported FTIR spectra were collected once the sample was dried.

For metal coordination of **1 H**, a spatula of $CuCl_2$ salt was sprinkled onto the oligoamide deposit. A 20-μl aliquot of DI water was then deposited to fully hydrate the system. The same drying process as neat **1 H** was used to ensure a dry sample before data collection.

IR data analysis

The spectra were processed using the Bruker OPUS 7 spectroscopy software. Sample spectra were corrected against background measurements performed through the clean ATR crystal. Additional water vapor correction was performed by using a pure water vapor spectrum collected on the instrument. Spectra were plotted using a custom python script (Python Software Foundation. Python Language Reference, version 3.10.9) using the OPUSfc, matplotlib, and numpy packages. Spectra were further normalized and vertically shifted for ease of viewing.

Sample preparation for AFM and XPS

The oligoamides were synthesized in-house, using a published procedure.[22] Materials were stored, lyophilized, and dissolved as required. A solution of 3.25 mg/ml **1 H** oligoamide solution was prepared using DI water with resistivity 18.2 Mcm. Silicon wafer *p*-type doped, with a 2000 Å thermal oxide layer was purchased from Silicon Valley Microelectronics, Santa Clara, Calif., and were cut into 5-mm squares. The wafers were cleaned with a procedure of 5-min sonication in de-ionized water, acetone, isopropanol, sequentially, then drying with a cleanroom wipe, Durx 670A, ISO 5-8. Substrates were ozone treated in a Novascan, Boone, Iowa, PSD pro UV Ozone cleaner, for 10 min. Oligoamide was drop-cast in 20-μl aliquots onto the silicon wafer. After 15 min, the excess oligoamide solution was removed with a pipette.

To coordinate the oligoamide, a 20-μl aliquot of metal–salt solution was deposited onto the neat **1 H** oligoamides and left for three hours. After removing excess solution a subset of samples were rinsed, by pipetting a 20-μl aliquot of de-ionized water onto the sample that was then immediately removed.

XPS

XPS was performed on a Thermo Scientific Theta Probe system. The system was kept at base pressure of $\approx 5 \times 10^{10}$ mbar. The x-ray source was monochromated Al Kα (1486.7 eV). The x-ray spot size was 400 μm in diameter. The spectrometer was precalibrated by performing measurements on clean Ni, Au, Ag, and Cu standard samples, whereby the Ni Fermi edge, Au $4f_{7/2}$, Ag $3d_{5/2}$, and Cu $2p_{3/2}$ peaks were aligned to binding energies of 0.00 0.02 eV, 83.98 0.02 eV, 368.26 0.02 eV, and 932.67 0.02 eV, respectively. The full width at half maximum (FWHM) of the Ag $3d_{5/2}$ photoelectron peak was 0.5 eV. XPS spectra were recorded at a detection angle (q) of 50°, with respect to the sample surface. A hemispherical electron analyzer was used to detect the photoelectrons, it was set to a pass energy of 150 eV for survey spectra and 40 eV for the core level spectra. To eliminate any positive charge-induced binding energy shift, a low energy electron flood gun was used for charge compensation during spectrum acquisition. The XPS spectra reported here are referenced to advantageous sp^3 hybridized carbon signal, which was prevalent in all samples.

Analysis

The XPS data were processed using CasaXPS version 2.3.24rev1.1Z. All high-resolution principle photoemission scans were curve fit with Lorentzian Gaussian line shapes at a ratio of 30%, 70% Gaussian and 30% Lorentzian (GL[30]). The position of the corresponding Auger peak was also fitted with a GL(30) under a Shirley background region. For the Auger electron peaks, the FWHM was unconstrained to allow for the broad nature of Auger electron energies to be accounted for with multiple peaks fitted only where appropriate. The XPS measurements of **1 H** + Cu were also compared with the addition of glutamic acid and imidazole to $CuCl_2$. As these are the binding moieties of interest within **1 H** as previously identified.[23]

Wagner plots provide information about the local chemical environment experienced by the core-ionized element of interest.[34] The Wagner plot was produced by plotting each sample's photoelectron $2p_{3/2}$ binding energy against the corresponding Auger $L_3M_{4,5}M_{4,5}$ kinetic energy peak position, to produce a scatter plot. This methodology has been employed previously for distinguishing chemical environments within MSFs[2].

AFM

AFM for the **1 H** was performed on a Veeco (Plainview, N.Y.), Dimension 3100, in semicontact mode. AFM tips used were Bruker TESP-V2, with a spring constant of 42 N/m, no front or back coating. Measurements were performed in a C100 cleanroom under ambient conditions. Images were captured at a resolution of 512 × 512 and at a scan rate of 0.8–1.2 Hz.

AFM for the **1 H** + Cu was performed on a NT-MDT, NTEGRA system, Moscow, in semicontact mode, using NT-MDT NSG30 probes, with a nominal force constant of 22-100 N/m with a gold reflective coating. Measurements were performed under ambient conditions. Images were captured at a resolution of 1024 × 1024 or 512 × 512, and at a scan rate of 0.8–1.5 Hz.

Measurements were collected in triplicates across each sample's surface; with corresponding microscope images taken to identify the landing zone of the probe. The images presented in this manuscript are representative of consistent structures found across the sample.

AFM image processing

Gwyddion version 2.60 was used to process the AFM images http://gwyddion.net/. Leveling data by mean plane subtraction and align rows using median of differences was first used to determine the features present within the sample. For publication the AFM scans were processed through aligning the rows by crossing lines, then using three-point plane fit to appropriately flatten the image. To remove high structures by threshold, the height of the mask was set to an appropriate height. Then the data under the mask were interpolated by solution of Laplace equation.

SAXS

All SAXS measurements were undertaken on the SAXS/WAXS beamline[39] using x-ray energy of 11.5 keV or 1.078 Å, at the Australian synchrotron, part of ANSTO. **1 H** was measured at a concentration of 1 mg/ml in H_2O. A **1 H** + Cu(II) solution was prepared by mixing equal amounts of this **1 H** solution and a 2-mmol $CuCl_2$ to create a 0.5-mg/ml **1 H** in 1-mmol Cu(II) solution, and allowed to rest 15 min before measurement. Samples were introduced to the beam in 1-mm quartz capillaries using the in-house automated capillary sampler, and the 2D scattering patterns were collected on the detector (Pilatus 1 M, Dectric, Baden) at a distance of 2.7 m from the sample. Data were reduced to an intensity versus scattering vector (Q) plot using ScatterBrain[40] software (Australian Synchrotron) with a water-filled capillary as the blank, and normalized to an absolute scale with water. SASView[41] (http://www.sasview.org/) software was used to model SAXS data from the two samples. A composite model of two elliptical cylinders[42,43] was applied to the data, Equation (SA1), providing average length and radii values for two populations in each sample.[43] Details relating to model fitting can be found in the Supplementary information.

STM

Scans were taken with a SPECS Aarhus STM with spring-mounted internal vibration damping and a tungsten wire tip. Measurements were performed under ultrahigh vacuum (UHV) (10^{-10} Torr). Tip improvement was done on graphite before the first set of scans. Bias voltages of 0.5–1 V and set points of 0.7–1.5 nA were used, values optimized for best surface tracking.

Initial deposition

0.5 µL of 100 mM **1 H** oligoamide were drop-cast onto a boron-doped C(100) diamond with hydrogen passivation. The deposit was rinsed with water and allowed to dry. The sample was introduced to UHV and annealed at 54°C overnight before STM scans were taken.

Copper coordination

The sample was removed from UHV and two 0.5-µL aliquots of 50-µM $CuCl_2$ solution were added on subsequent days. The sample was rinsed with water, then a further 4 µL of 50-µM $CuCl_2$. The sample was reintroduced to UHV and annealed at 54°C overnight before STM scans were taken.

Substrate choice

A variable that changes across this multi-technique study is the substrate, which was chosen in each case to match specific experimental considerations for that technique; unfortunately, it was not possible to find a single substrate material that would meet the requirements in every single case while also being only weakly interactive with the fibers. For the subsequent XPS and AFM analysis, a conductive but nearly atomically flat substrate was required to meet the criteria of both XPS and AFM. We have performed morphology characterization on each XPS sample to ascertain homogeneous surface coverage and the presence of structured (i.e., metal cross-linked material). Mica, while atomically flat, is not conductive and as such is a poor substrate for XPS analysis. Gold and graphite are conductive; however, they are not flat. Consistently doped silicon was chosen as a substrate for these measurements, as it allows for the conductivity required by XPS measurements to prevent charging, and is flat enough to produce sufficient AFM images. Hydrogen-terminated diamond was used as a substrate for the STM due to its advantageous surface chemistry, compatible conductivity, and smooth morphology. Metal surfaces such as gold interfere with the coordination process, and graphite was found not conductive enough, therefore, we chose H-terminated diamond that is routinely used for STM in-house. For FT-IR experiments, silicon ATR crystal was used. SAXS was performed in solution without a substrate support. Given that the substrate is supposed to have minimal interference with the self-assembling properties of **1 H** + Cu, the driving self-assembly motifs of hydrogen bonding and metal coordination are not expected to have a significant impact on the behavior of **1 H** + Cu in this study.

Acknowledgments

Part of this work was supported by La Trobe University and the Agency for Science, Technology and Research (A*STAR) Institute of Materials Research and Engineering (IMRE) under the A*STAR Research Attachment Programme (ARAP). This work was performed in part at A*STAR's IMRE in Singapore. We thank ANSTO for the allocation of beamtime. Part of this research was undertaken on the SAXS/WAXS beamline at the Australian Synchrotron, part of ANSTO. This work benefited from the use of the SasView application, originally developed under NSF Award No. DMR - 0520547. SasView also contains code developed with funding from the EU Horizon 2020 Programme under the SINE2020 Project Grant No. 654000. We thank HZB for the allocation of synchrotron radiation beamtime. Measurements were carried out at the IRIS beamline at the BESSY II electron storage ring operated by the Helmholtz-Zentrum Berlin für Materialien und Energie. We thank the National Computational Infrastructure National Facility (NCI-NF), Intersect, and La Trobe University for high-performance computing resources.

Author contributions

The conceptual design of this work was devised by A.M. and N.W. C.B. performed and analyzed the SAXS experiments, with conceptualization assistance from C.G. A.M. performed QTAIM simulations and corresponding interpretation, with assistance from D.W. R.G. performed the STM data collection and analysis. Interpretation of STM was devised by R.G., A.M., A.S., C.P., and N.W. IR, AFM, and XPS experiments were designed and performed by N.W. Analysis and interpretation of IR was assisted by L.P. Analysis and interpretation of the XPS was assisted by D.Q., J.P., and A.S. The experimental parts of the manuscript were written by authors of respective expertise and assembled by N.W. with feedback from all authors.

Funding

Open Access funding enabled and organized by CAUL and its Member Institutions. Part of this work was supported by La Trobe University and the Agency for Science, Technology and Research (A*STAR) Institute of Materials Research and Engineering (IMRE) under the A*STAR Research Attachment Programme (ARAP). Part of this research was undertaken on the SAXS/WAXS beamline at the Australian Synchrotron, part of ANSTO. This work benefited from the use of the SasView application, originally developed under NSF Award No. DMR - 0520547. SasView also contains code developed with funding from the EU Horizon 2020 Programme under the SINE2020 Project Grant No. 654000. We thank HZB for the allocation of synchrotron radiation beamtime. Measurements were carried out at the IRIS beamline at the BESSY II electron storage ring operated by the Helmholtz-Zentrum Berlin für Materialien und Energie. We thank the National Computational Infrastructure National Facility (NCI-NF), Intersect, and La Trobe University for high-performance computing resources.

Data availability

Data are available from the corresponding authors upon request.

Conflict of interest

The authors have no conflict of interest to declare that are relevant to the content of this article.

Appendix A: Supplementary information

The SAXS data processing in Scatterbrain involved normalization to an absolute scale as shown by Equation (SA1), where *I*, water at 20 Cdeg is 1.641×10^{-2} cm^{-1}. The model fitting performed in SASView was completed on the premise that the dominating scattering at such dilute concentrations is due to the form factor, and therefore, allowing an average morphological envelope of the structures present in water to be modeled.

Equations:

$$I(\vec{q}) = \frac{\text{Scale}}{V}\int_0^{\frac{\pi}{2}} \Phi^2(qr)\delta\alpha + \text{Background} \qquad \text{A1}$$

$$\text{Where; } \Phi^2(qr) = \frac{J_1(a)sin(b)}{ab} \qquad \text{A2}$$

$$a = qr'sin\alpha \qquad \text{A3}$$

$$a = q\frac{L}{2}cos\alpha \qquad \text{A4}$$

$$r' = \frac{r_{minor}}{\sqrt{2}}\sqrt{(1 + V^2) + (1 - V^2)cos\psi} \qquad \text{A5}$$

$$V = \frac{4}{3}\pi \times r_{minor} \times r_{major} \times L \qquad \text{A6}$$

where J_1 is the first order Bessel function, q is the scattering vector, V = volume and L = length.

$$\Delta I_{Abs}(q) = \frac{\Delta I(q)}{\Delta I_{H_2O}} \times I_{\mathrm{H_2O20^\circ C}} \qquad \text{A7}$$

where

$$I_{\mathrm{H_2O20^\circ C}} = 1.641 \times 10^{-2}\mathrm{cm}^{-1}. \qquad \text{A8}$$

Open Access

References

1. S.H. Gellman, *Acc. Chem. Res.* **31**(4), 173 (1998). https://doi.org/10.1021/ar960298r
2. N.G. West, S.E. Bamford, P.J. Pigram, J. Pan, D.C. Qi, A. Mechler, *Mater. Horiz.* **10**(12), 5584 (2023). https://doi.org/10.1039/D3MH01327H
3. D.H. Appella, L.A. Christianson, I.L. Karle, D.R. Powell, S.H. Gellman, *J. Am. Chem. Soc.* **118**(51), 13071 (1996). https://doi.org/10.1021/ja963290l
4. M. Kajtár, M. Hollósi, G. Snatzke, *Tetrahedron* **27**(22), 5659 (1971). https://doi.org/10.1016/S0040-4020(01)91731-4
5. D. Seebach, D.F. Hook, A. Glättli, *Biopolymers* **84**(1), 23 (2005). https://doi.org/10.1002/bip.20391
6. L.M. Johnson, S.H. Gellman, *Methods Enzymol.* **523**, 407 (2013). https://doi.org/10.1016/B978-0-12-394292-0.00019-9
7. K. Luder, K. Kulkarni, H.W. Lee, R.E. Widdop, M.P. Del Borgo, M.I. Aguilar, *Chem. Commun.* **52**(24), 4549 (2016). https://doi.org/10.1039/C6CC00247A
8. M.P. Del Borgo, K. Kulkarni, M.I. Aguilar, *Aust. J. Chem.* **70**(2), 126 (2016). https://doi.org/10.1071/CH16511
9. M.P. Del Borgo, K. Kulkarni, M.A. Tonta, J.L. Ratcliffe, R. Seoudi, A.I. Mechler, P. Perlmutter, H.C. Parkington, M.-I. Aguilar, *APL Bioeng.* **2**(2), 026104 (2018). https://doi.org/10.1063/1.5020105
10. C.M. Goodman, S. Choi, S. Shandler, W.F. DeGrado, *Nat. Chem. Biol.* **3**(5), 252 (2007). https://doi.org/10.1038/nchembio876
11. T.A. Martinek, F. Fülöp, *Chem. Soc. Rev.* **41**(2), 687 (2012). https://doi.org/10.1039/C1CS15097A
12. R.P. Cheng, S.H. Gellman, W.F. DeGrado, *Chem. Rev.* **101**(10), 3219 (2001). https://doi.org/10.1021/cr000045i
13. Y.D. Wu, W. Han, D.P. Wang, Y. Gao, Y.L. Zhao, *Acc. Chem. Res.* **41**(10), 1418 (2008). https://doi.org/10.1021/ar800070b
14. K. Kulkarni, N. Habila, M.P. Del Borgo, M.I. Aguilar, *Front. Chem.* **7**, 70 (2019). https://doi.org/10.3389/fchem.2019.00070
15. A.J. Christofferson, Z.S. Al-Garawi, N. Todorova, J. Turner, M.P. Del Borgo, L.C. Serpell, M.I. Aguilar, I. Yarovsky, *ACS Nano* **12**(9), 9101 (2018). https://doi.org/10.1021/acsnano.8b03131
16. R.S. Seoudi, M.G. Hinds, D.J.D. Wilson, C.G. Adda, M. Del Borgo, M.I. Aguilar, P. Perlmutter, A. Mechler, *Nanotechnology* **27**(13), 135606 (2016). https://doi.org/10.1088/0957-4484/27/13/135606
17. R.S. Seoudi, A. Dowd, B.J. Smith, A. Mechler, *Phys. Chem. Chem. Phys.* **18**(16), 11467 (2016). https://doi.org/10.1039/C6CP01355D
18. R.S. Seoudi, A. Dowd, M. Del Borgo, K. Kulkarni, P. Perlmutter, M.I. Aguilar, A. Mechler, *Pure Appl. Chem.* **87**(9–10), 1021 (2015). https://doi.org/10.1515/pac-2015-0108
19. R.S. Seoudi, M.P. Del Borgo, K. Kulkarni, P. Perlmutter, M.I. Aguilar, A. Mechler, *New J. Chem.* **39**(5), 3280 (2015). https://doi.org/10.1039/C4NJ01926A
20. C. Buchanan, M.G. Hinds, L. Puskar, C.J. Garvey, A. Mechler, *Pure Appl. Chem.* **93**(11), 1327 (2021). https://doi.org/10.1515/pac-2021-0324
21. C. Buchanan, "Hierarchical Self-Assembly of Substituted Oligoamides," PhD thesis, La Trobe University (2022). https://doi.org/10.26181/21061750.v1
22. M.P. Del Borgo, A.I. Mechler, D. Traore, C. Forsyth, J.A. Wilce, M.C.J. Wilce, M.I. Aguilar, P. Perlmutter, *Angew. Chem. Int. Ed.* **52**(32), 8266 (2013). https://doi.org/10.1002/anie.201303175
23. N.G. West, R.S. Seoudi, A.J. Barlow, D. Qi, L. Puskar, M.P. Del Borgo, K. Kulkarni, C.G. Adda, J. Pan, M.I. Aguilar, P. Perlmutter, A. Mechler, *Mater. Adv.* **1**(5), 1134 (2020). https://doi.org/10.1039/D0MA00123F
24. C. Buchanan, C.J. Garvey, L. Puskar, P. Perlmutter, A. Mechler, *Supramol. Chem.* **32**(3), 222 (2020). https://doi.org/10.1080/10610278.2020.1730839
25. C.F. Meares, Peptide–Metal Interactions in *Encyclopedia of Inorganic and Bioinorganic Chemistry*, ed. by R.A. Scott (Wiley, Chichester, 2011), pp. 1–14. https://doi.org/10.1002/9781119951438.eibc0167
26. M.T. Carroll, C. Chang, R.F. Bader, *Mol. Phys.* **63**(3), 387 (1988). https://doi.org/10.1080/00268978800100281
27. W. Nakanishi, S. Hayashi, K. Narahara, *J. Phys. Chem. A* **112**(51), 13593 (2008). https://doi.org/10.1021/jp8054763
28. H. Fabian, W. Mäntele, "Infrared Spectroscopy of Proteins," in *Handbook of Vibrational Spectroscopy* (Wiley, 2002)
29. A. Barth, *Biochim. Biophys. Acta Bioenerg.* **1767**(9), 1073 (2007). https://doi.org/10.1016/j.bbabio.2007.06.004
30. Y. El Khoury, P. Hellwig, *J. Biol. Inorg. Chem.* **14**(1), 23 (2009). https://doi.org/10.1007/s00775-008-0421-4
31. M.C. Biesinger, *Surf. Interface Anal.* **49**(13), 1325 (2017). https://doi.org/10.1002/sia.6239
32. C. Wagner, A. Joshi, *J. Electron Spectrosc. Relat. Phenom.* **47**, 283 (1988). https://doi.org/10.1016/0368-2048(88)85018-7
33. A.V. Naumkin, A. Kraut-Vass, S.W. Gaarenstroom, C. Powell. X-ray Photoelectron Spectroscopy Database. NIST Standard Reference Database 20, XPS,Version 4.1 (2012). https://doi.org/10.18434/T4T88K
34. G. Moretti, *J. Electron Spectrosc. Relat. Phenom.* **95**(2–3), 95 (1998). https://doi.org/10.1016/S0368-2048(98)00249-7
35. J. Butler, Y.A. Mankelevich, A. Cheesman, J. Ma, M. Ashfold, *J. Phys. Condens. Matter* **21**(36), 364201 (2009)
36. L.-M. Yang, T. Frauenheim, E. Ganz, *J. Nanomater.* **2016**, 8429510 (2016). https://doi.org/10.1155/2016/8429510
37. M.J. Frisch, G.W. Trucks, H.B. Schlegel, G.E. Scuseria, M.A. Robb, J.R. Cheeseman, G. Scalmani, V. Barone, B. Mennucci, G.A. Petersson, H. Nakatsuji, M. Caricato, X. Li, H.P. Hratchian, A.F. Izmaylov, J. Bloino, G. Zheng, J.L. Sonnenberg, M. Hada, M. Ehara, K. Toyota, R. Fukuda, J. Hasegawa, M. Ishida, T. Nakajima, Y. Honda, O. Kitao, H. Nakai, T. Vreven, J.A. Montgomery Jr., J.E. Peralta, F. Ogliaro, M. Bearpark, J.J. Heyd, E. Brothers, K.N. Kudin, V.N. Staroverov, R. Kobayashi, J. Normand, K. Raghavachari, A. Rendell, J.C. Burant, S.S. Iyengar, J. Tomasi, M. Cossi, N. Rega, J.M. Millam, M. Klene, J.E. Knox, J.B. Cross, V. Bakken, C. Adamo, J. Jaramillo, R. Gomperts, R.E. Stratmann, O. Yazyev, A.J. Austin, R. Cammi, C. Pomelli, J.W. Ochterski, R.L. Martin, K. Morokuma, V.G. Zakrzewski, G.A. Voth, P. Salvador, J.J. Dannenberg, S. Dapprich, A.D. Daniels, O. Farkas, J.B. Foresman, J.V. Ortiz, J. Cioslowski, D.J. Fox. Gaussian 09, Revision B.01 (Gaussian Inc., Wallingford, 2016)
38. T.A. Keith, Keith AIMAll (n.d.) aim.tkgristmill.com
39. N.M. Kirby, S.T. Mudie, A.M. Hawley, D.J. Cookson, H.D.T. Mertens, N. Cowieson, V. Samardzic-Boban, *J. Appl. Crystallogr.* **46**(6), 1670 (2013). https://doi.org/10.1107/S002188981302774X.
40. http://archive.synchrotron.org.au/aussyncbeamlines/saxswaxs/software-saxswaxs
41. M. Doucet, J.H. Cho, G. Alina, Z. Attala, J. Bakker, W. Bouwman, P. Butler, K. Campbell, T. Cooper-Benun, C. Durniak, L. Forster, M. Gonzalez, R. Heenan, A. Jackson, S. King, P. Kienzle, J. Krzywon, R. Murphy, T. Nielsen, L. O'Driscoll, W. Potrzebowski, S. Prescott, R. Ferraz Leal, P. Rozyczko, T. Snow, A. Washington. SasView Version 5.0.4, *Zenodo* (2021). https://doi.org/10.5281/zenodo.4467703
42. L. Onsager, *Ann. N.Y. Acad. Sci.* **51**(4), 627 (1949). https://doi.org/10.1111/j.1749-6632.1949.tb27296.x
43. L.A. Feigin, D.I. Svergun, *Structure Analysis by Small-Angle X-Ray and Neutron Scattering* (Springer, Cham, 1987). https://doi.org/10.1007/978-1-4757-6624-0

Publisher's note